Experimental investigation and constitutive modelling of the mechanical and ratcheting properties in rail steels

Ren, Fang; Yang, Zhen; Li, Zili

DOI
10.1093/iti/liaf011

Publication date
2025

Document Version
Final published version

Published in
Intelligent Transportation Infrastructure

Citation (APA)
Ren, F., Yang, Z., & Li, Z. (2025). Experimental investigation and constitutive modelling of the mechanical and ratcheting properties in rail steels. *Intelligent Transportation Infrastructure*, *4*, Article liaf011. https://doi.org/10.1093/iti/liaf011

OXFORD

Intelligent Transportation Infrastructure, 2025, liaf011

https://doi.org/10.1093/iti/liaf011

Research Article

Experimental investigation and constitutive modelling of the mechanical and ratcheting properties in rail steels

Fang Ren, Zhen Yang, Zili Li*

Railway Engineering, Engineering Structures, Delft University of Technology, Stevinweg 1, 2628 CN, Delft, The Netherlands

*Corresponding author. Delft University of Technology, Stevinweg 1, 2628 CN, Delft, The Netherlands. E-mail: Z.Li@tudelft.nl

The ratcheting phenomenon remains a persistent concern in modern railways due to its close association with head checks, a typical type of rolling contact fatigue. This study presents experimental research focussing on elucidating the mechanical, hardening, and material ratcheting properties of one bainitic (B320) and two pearlitic (R220 and R260MN) rail steels. The experiment consisted of monotonic tension, uniaxial cyclic strain range, and uniaxial cyclic stress range tests. Two load cases representing the equivalent stresses experienced by rails under real-life wheel–rail contacts were used in the cyclic stress range tests to assess the rail ratcheting behaviour in railway operating conditions. The test results highlighted that the two pearlitic steels showed similar mechanical strength and ratcheting behaviour; and by contrast, the bainitic steel exhibited superior mechanical strengths and yielded significantly weaker ratcheting responses for both load cases. The study then characterised the three rail steels by calibrating for them the hardening parameters of two classical constitutive models: Chaboche and Ohno-Wang II (OWII) based on the monotonic and cyclic strain range tests. The hardening parameters of the constitutive models were then optimied based on the cyclic stress range tests to represent the material ratcheting behaviours of rail steels for each load case. Notably, the OWII model demonstrated higher precision in reproducing ratcheting strains and rates than the Chaboche model, which faced limitations in simulating relatively low ratcheting rates. This study enhanced the understanding of the mechanical and ratcheting properties of the investigated rail steels and provided insights into the applicability of constitutive models for predicting and mitigating rail ratcheting effects.

Keywords: material ratcheting; bainitic and pearltic rail steels; cyclic testing; constitutive modelling; wheel–rail contact.

1. Introduction

Head check (HC), a typical type of rolling contact fatigue (RCF), poses a persistent challenge in modern railway systems. HC originates from frictional contact at the wheel–rail interface (Bower and Johnson 1989, 1991). Repeated loading and unloading of wheels create cyclic contact stresses on the rails, and cause rail ratcheting, that is progressive accumulation of plastic strain in the rails RCF (Bower and Johnson 1989; Paul 2019). When the accumulated plastic strain exceeds the ductility limit of the rail steel, cracks initiate in the severely deformed layer in the rail surface or subsurface (Donzella 2005; Fletcher et al., 2009). Therefore, understanding the ratcheting behaviour of rail steels is desirable for investigating HC damage in rails.

The rail ratcheting can be classified into material and structural ratcheting (Hübel 1996; Paul 2019). Material ratcheting, an intrinsic elastoplastic behaviour of steels, can be observed in a cyclic tension–compression test that proportionally and homogeneously loads samples under asymmetrical stress conditions (Bari and Hassan 2000; Paul 2019), whereas structural ratcheting is related to the plastic strain accumulated in the non-uniformly distributed and altering stress conditions during cyclic loading. At the wheel–rail interface, the structural ratcheting is marked by the changing contact stresses as a result of evolving contact geometry in relation to the material ratcheting (Ren et al., 2024), with the material ratcheting induced by the asymmetric loading and unloading from the repeated wheel passages (Pun 2015; Wu 2023; Ren et al., 2024). Although both ratcheting forms are significant in rail steels, this study focussed primarily on the material ratcheting, which is essential to define rail properties in the RCF-related ratcheting studies RCF (Bower and Johnson 1989; Tyfour et al., 1996; Ringsberg 2000; Pun 2015; Pletz 2019; Su 2019; Wu 2023; Ren et al., 2024; Wu 2024). Moreover, material ratcheting in rail steels, induced by the loading and unloading of contact stresses, causes the accumulation of plastic deformation in the rail surface. Consequently, the accumulation of plastic deformation alters contact profiles and causes structural ratcheting (Ren et al., 2024), which thus creates an interplay between the two ratcheting processes. Therefore, understanding the material ratcheting of rail steels is crucial as the first step towards a better understanding of the complete ratcheting effects in rails.

To reproduce material ratcheting in rail steels, constitutive models that can capture the hardening processes of rail materials and characterise their elastoplastic behaviours are needed (Chaboche 1986 1991; Ohno and Wang 1993; Jiang and Sehitoglu 1996; Kang and Gao 2002; Frederick and Armstrong 2007; Abdel-Karim 2009). Most of the proposed constitutive models aimed to identify a single set of hardening parameters, to describe ratcheting behaviours across predefined general loading patterns in tension–compression tests. This approach, however,

---

Received: January 19, 2025. **Revised:** May 15, 2025. **Accepted:** May 22, 2025

resulted in complex constitutive models, raising a concern about computational efficiency when applied to numerical cyclic contact simulations, particularly when using the finite element (FE) method to simulate a large number of wheel–rail contacts (Ren et al., 2024). Furthermore, general loading patterns in the uniaxial tension–compression tests might not align well with the specific loading and unloading patterns of the wheel–rail contact stresses in railway operating conditions. This mismatch may reduce the effectiveness of these models in approximating the ratcheting effects in the rails. To study the ratcheting effects in rails more efficiently and effectively under cyclic wheel–rail contacts over a high number of cycles (Ren et al., 2024), it is beneficial to calibrate well-established and less complex constitutive models such as the Chaboche and OWII models to reproduce the material ratcheting of rail steels. In addition, it is also essential to optimise their hardening parameters for specific load cases that closely resemble real-life wheel–rail contacts in railway operating conditions.

To calibrate the constitutive models for rail steels, their mechanical and hardening properties need to be identified through experimental investigations. Pearlitic rail steels have been widely used in modern railway systems, leading to numerous tests to investigate their mechanical properties and resistance to RCF (Tyfour et al., 1996; Eadie 2008; Stock and Pippan 2011; Athukorala et al., 2016; Hu 2021). To improve the RCF resistance of the rails, bainitic rail steels have recently been introduced. Although it has not yet been widely applied in the field, its mechanical properties and microstructure have been evaluated in various tests and compared to pearlitic steels (Hasan et al., 2018; Hajizad 2019; Lesage 2022). However, existing research focused qualitatively on RCF damage and resistance through roller-rig tests (Tyfour et al., 1996; Stock and Pippan 2011), field observations (Stock and Pippan 2011; Zhou 2014), and microscopic analyses (Hu 2021; Lesage 2022), but few experimental investigations addressed the rail material ratcheting behaviours via cyclic tension–compression tests and the subsequent analysis of their hardening characteristics, especially for bainitic rail steels. This underscores the need for more in-depth experimental investigation and constitutive modelling to understand the elasto-plastic properties of rail steels on a macro scale and to provide quantitative insights into their ratcheting behaviours relevant to their RCF resistance. Additionally, comparing bainitic steels with the traditionally-used pearlitic steels may show the benefits of bainitic steels in terms of RCF resistance for future large-scale railway applications.

This study focused on testing, characterising, and comparing the mechanical and material ratcheting properties of two pearlitic rail steels used in the Dutch metro (R220) and railway (R260MN), along with a new bainitic rail steel (B320). The experimental investigation was conducted in three stages: monotonic tension, uniaxial cyclic strain range, and uniaxial cyclic stress range tests. The results of the former two tests formed the basis for calibrating the Chaboche and OWII constitutive models to account for the non-linear kinematic hardening (NLKH) and isotropic hardening properties of the steels. The initially calibrated constitutive models were further optimised for the material ratcheting behaviours of the rail steels by considering stresses induced by real-life wheel–rail contact in railway operating conditions, in the cyclic stress range test. Finally, this study compared the results of the ratcheting simulations using the optimised constitutive models across the different rail steels.

2. Experimental investigation

This section explained the design, load cases, and outcome of the experiment investigation. Three tests were performed sequentially at three stages: monotonic tension tests, uniaxial cyclic strain range tests, and uniaxial cyclic stress range tests, to examine the mechanical, hardening, and ratcheting properties of the rail steels of interest, respectively. The test results were also compared and discussed.

2.1. Test design and load case

The chemical compositions of the rail steels tested in this study are detailed in Table 1. Test samples of these rails were carefully fabricated from the real-life rail head, as illustrated in Fig. 1a. The test specimens were cut 1 mm below the original rail surface to align closely with the material properties of rail top surface, where wheel–rail contact predominantly occurs. The dimensions of the test samples are detailed in Fig. 1b. The uniaxial tension–compression tests were conducted on a specialised in-house fatigue test machine with a 100 kN gripping capacity, capable of delivering up to 60 kN of both tension and compression forces. An MTS axial dynamic extensometer was used to measure the axial strain up to 20%. Furthermore, all tests were conducted under the room temperature ($15^\circ - 25^\circ$C) with no further environmental control applied. The test specimens were loaded with a maximum strain rate of 0.1 $\%s^{-1}$ to limit the time-dependent strain rate effects (Pun 2014).

The experiment investigation was conducted at three stages, with the tests and processes outlined in Fig. 2. At Stage 1, the samples were loaded monotonically in tension until fracture to obtain mechanical properties, including Young's modulus E, the 0.2%-offset yield strength (OYS) R_y, the ultimate strength Rm, and toughness (area under the stress–strain curve, see Fig. 3). The tests were performed at least three times per rail steel to account for variations in these parameters. Elastic limits were also obtained at the upper boundary of the elastic range within the stress-strain curve. Elastic limits are generally lower than OYS and applied as yield stresses σ_y in constitutive models (Chaboche 1986; Ohno and Wang 1993) to accurately capture the elastic response of the material (as demonstrated in 3)).

At Stage 2, cyclic tests with a symmetric loading pattern were performed within a ±1% strain range at a strain rate of 0.1 $\%\mathbf{s}^{-1}$. Each sample was tested for 100 cycles with the isotropic hardening saturated and kinematic hardening stabilised in plastic shakedown (Pun 2014; Paul 2019)(theoretical background and explanation in Sections 3 and 4.1). Based on the results of the stabilised cycle and the monotonic tension test, the initial NLKH and isotropic hardening parameters of constitutive models can be calibrated for the rail steels (Bari and Hassan 2000) (presented in Sections 3 and 4). In addition, to determine the load cases for the cyclic stress range test at Stage 3, that is the stress ranges that may induce rail ratcheting behaviours in real-life railway operating conditions, wheel–rail contact simulations were performed using an FE model (Ren et al., 2024) with the initial calibrated hardening parameters, as indicated in Fig. 2. Two load cases were determined to represent partial- and full-slip contact conditions, respectively, for all three rails, as to be elaborated in Section 4.3.

Cyclic stress range tests were performed at Stage 3 in which the samples were loaded and unloaded over 300 cycles. The two load cases LC1 and LC2 are presented in Table 2. The load cases comprise peak and residual stresses indicating the stress levels when the samples are loaded and unloaded.

Table 1. Chemical composition of the three rail steels. Information of R220 and R260MN is from batch specification, and B320 from (Lesage 2022).

Steel grade	C [%]	Si [%]	Mn [%]	P [%]	S [%]	Al [%]	Cr [%]	Cu [%]	Mo [%]	Ni [%]
R220	0.58	0.26	1.03	0.013	0.024	0.001	0.03	0.01	0.003	0.003
R260MN	0.65	0.31	1.39	0.010	0.012	0.001	0.03			0.020
B320	0.13–0.27	1.00–1.50	1.35–1.75	≤ 0.025	≤ 0.025	≤ 0.004	0.30-0.70	≤ 0.15	0.10–0.30	≤ 0.100

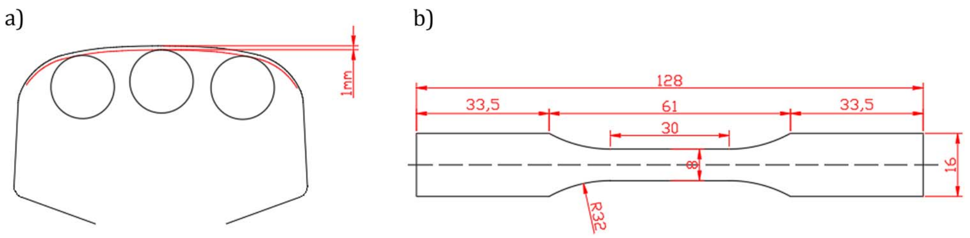

Figure 1 Design of the test sample: (a) the location of sample cutting from the original rail profile, and (b) dimension of the samples

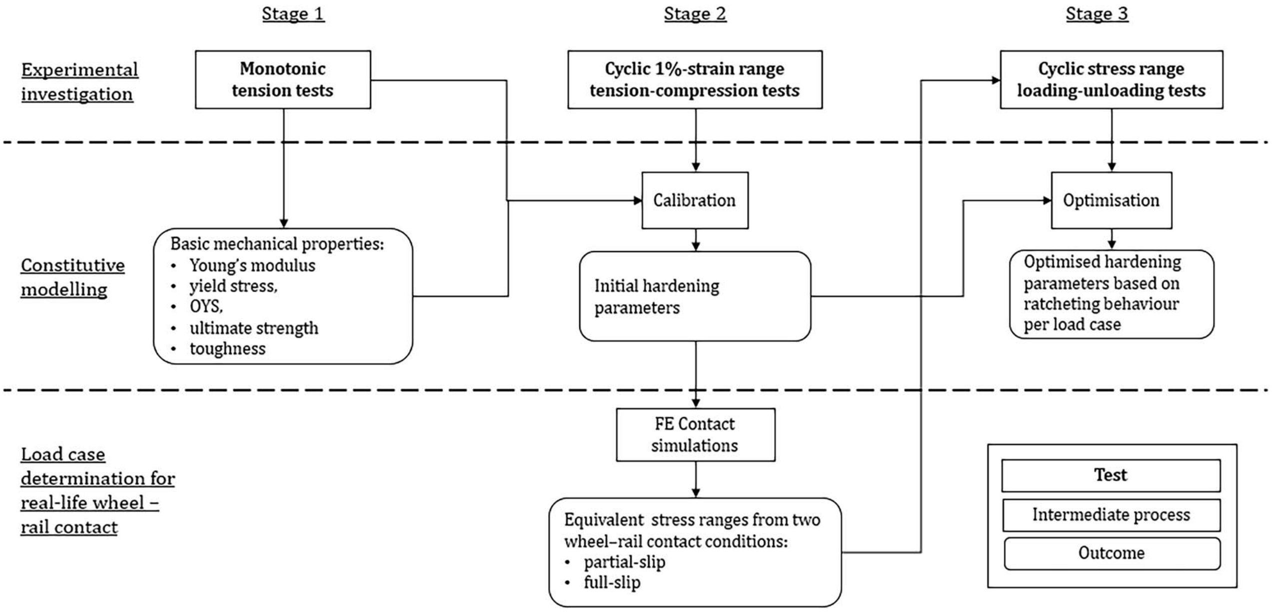

Figure 2 Overview of the experimental investigation at three stages, the consititutive modelling and the outcomes

LC2 has larger stress ranges (peak minus residual stress) than LC1 and higher level of means stresses as shown in Table 2. The loading-unloading patterns result in mean stresses of the asymmetrical stress ranges that can induce material ratcheting behaviour of the rail steels (Bari and Hassan 2000; Paul 2019). The analysis at this stage facilitated the optimisation of the hardening parameters obtained from Stage 2, based on wheel-rail contact simulations, to closely capture the material ratcheting behaviour of the rail steels, which were elaborated in Section 5.

2.2. Monotonic tension test

The results of the monotonic tension test conducted on the three rail steels are shown in Fig. 3 with the elastic limits (σ_y), OYS's (R_y), ultimate strengths (R_m) and fracture point indicated. The results show that among the rail steels tested, B320 has the highest OYS and ultimate strength of 870 MPa and 1,288 MPa, respectively. This aligns with the results reported in (Lesage 2022) that B320 has a much higher mechanical strength than R260 (similar to R260MN (Esveld 2001)). B320 also shows higher toughness than the two tested pearlitic steels. The mechanical properties obtained from the tests are summarised in Table 3, shown as mean values of the parameters with upper and lower bounds indicated in ± mean value.

2.3. Cyclic strain range test

The strain range test results at the 100th stabilised load cycle of the three rail steels are presented in Fig. 4. Figure 4a shows that the total strains fell within the ± 1% strain range required for the tests. Figure 4b indicates that B320 can achieve a high stress level of approximately ± 918 MPa within a relatively low plastic strain range of about ± 0.55%. This remarkable performance can be attributed to its superior mechanical strength, for example the high yield strength. In contrast, the R220 and R260MN steels behaved similarly with higher plastic strains at lower stress levels compared to B320. R260MN, with a stress level of 607 MPa and a plastic strain of 0.69%, marginally outperformed R220, with a stress level of 575 MPa at 0.71% plastic strain.

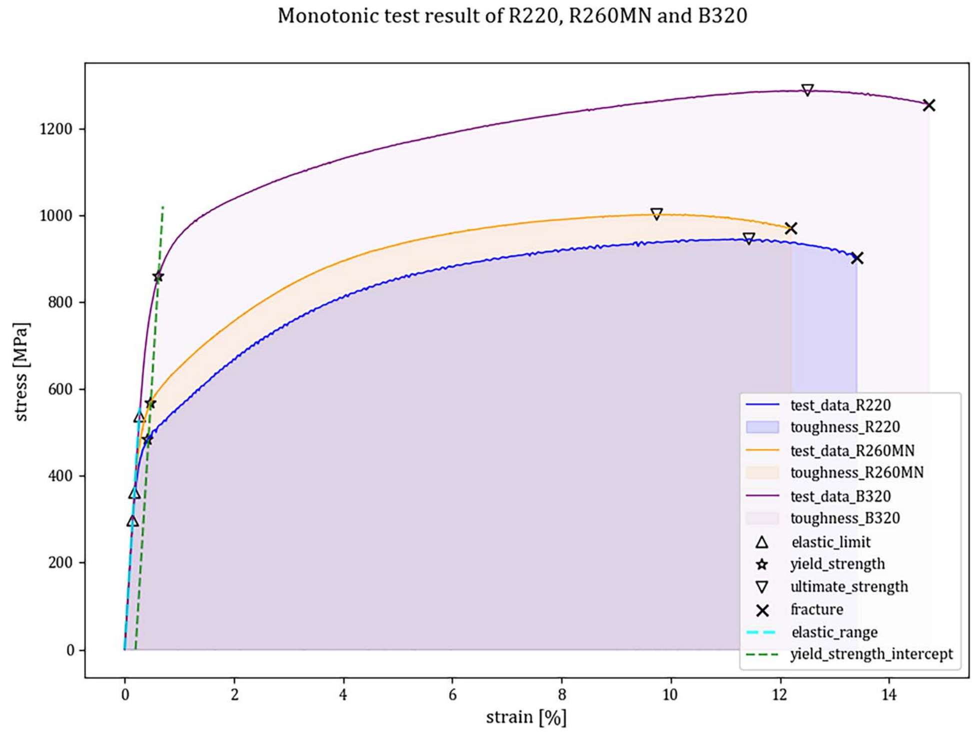

Figure 3 Monotonic behaviour of the tested rail steels (shown with the median values from the tests)

Table 2. Summary of load cases for cyclic stress ranges tests of Stage 3.

Load case	Steel grade [MPa]	R220	R260MN	B320
LC1	peak stress—loaded	570.0	617.0	880.0
	residual stress—unloaded	70.0	30.0	83.0
	mean stress	320.0	323.5	481.5
LC2	peak stress—loaded	770.0	820.0	1,015.0
	residual stress—unloaded	25.0	20.0	125.0
	mean stress	397.5	420.0	570.0

Table 3. Summary of the mechanical properties of the tested rail steels (average value provided).

Steel grade	Young's modulus [GPa]	Elastic limit [MPa]	0.2% OYS [MPa]	Ultimate strength [MPa]	Toughness [MJm^{-3}]
R220	200	290 ± 25	512 ± 22	946 ± 15	118 ± 15
R260MN	198	348 ± 20	568 ± 25	1, 022 ± 10	125 ± 12
B320	196	538 ± 35	870 ± 20	1, 288 ± 12	180 ± 30

2.4. Cyclic stress range test

Figure 5 presents the cyclic stress range test results for LC1. Among the three rail steels tested, R220 reached the highest ratcheting strain in the first cycle as shown in Fig. 5a, with both R220 and R260MN registering a total strain exceeding 1%. In contrast, B320 achieved a considerably lower strain of around 0.5% in the first cycle, despite being subjected to a higher stress level. Subsequent cycles reveal further ratcheting strain accumulation in R220 and R260MN, as shown in Fig. 5b, while B320 demonstrated limited accumulation. Overall, the ratcheting effects in LC1 were relatively modest for all three steels, with their ratcheting rates, that is change in ratcheting strain per cycle, rapidly reducing to very low levels, as illustrated in Fig. 5c. A small average ratcheting rate remains between 1.5×10^{-4}% and 2×10^{-4}% from 200 cycles on for R220 and R260MN, while that is nearly negligible about 4.24×10^{-5}% for B320. This trend is also visible in Fig. 5b as the curves of ratcheting strain for R220 and R260MN still show a small upward trend after 100 cycles, whereas it is almost flat for B320 from 20th cycle on. The results indicated the behaviour of the B320 steel resembled the elastic shakedown with no plastic strain accumulated after a few cycles (Bower and Johnson 1989; Tyfour et al., 1996; Paul 2019).

For the results of LC2 with larger stress ranges applied, more pronounced ratcheting effects can be observed. R220 and R260MN exhibited significant material ratcheting effects, as evidenced by a considerable accumulation of plastic strains, with their firstcycle plastic strain exceeding 2%, as illustrated in Fig. 6a. In contrast, B320 showed markedly less ratcheting effect, as shown

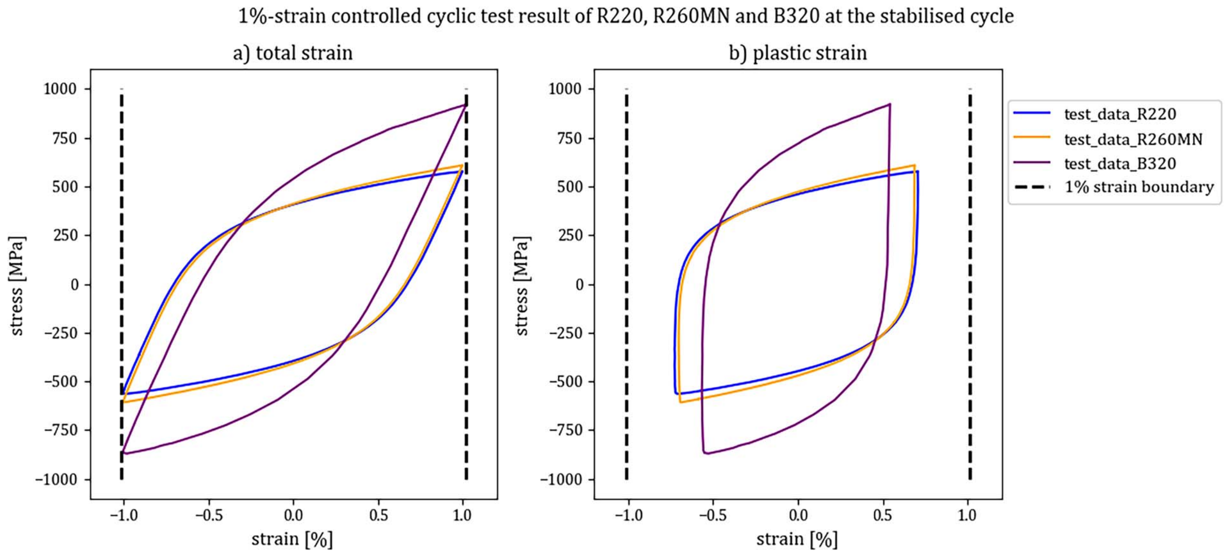

Figure 4 1% cyclic test results of the R220, R260MN and B320 rail steels: (a) stress–total strain plot at the stabilised 100th cycle, and (b) stress–plastic strain plot at the stabilised 100th cycle

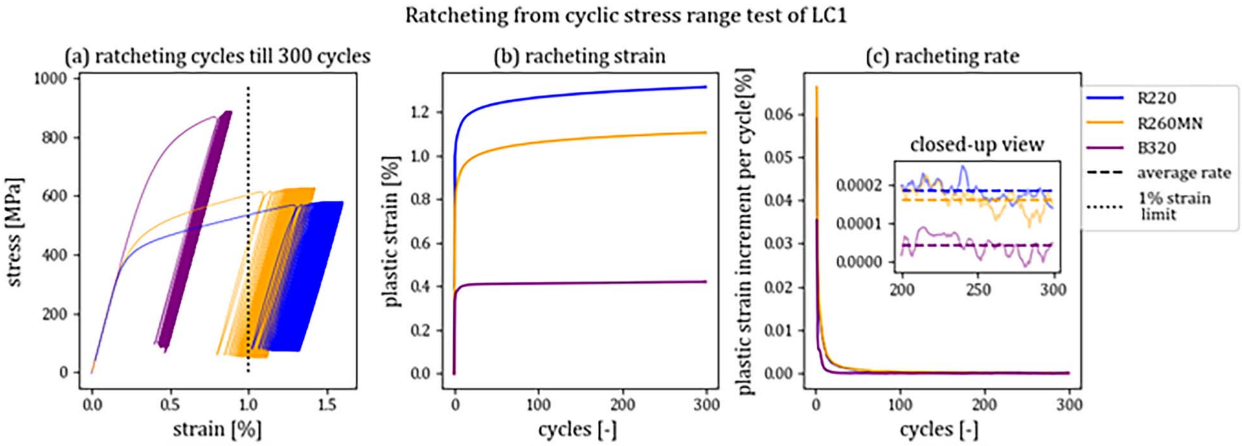

Figure 5 Cyclic stress range test results of the R220, R260MN and B320 rail steels for LC1: (a) stress-strain results till 300 cycles, (b) ratcheting strain plotted against load cycles, and (c) ratcheting rate plotted against load cycles

in Fig. 6a and b, with initial and final plastic strains below 1%. When comparing ratcheting rates, R220 and R260MN stabilised at about 0. 0075% and 0. 01%, respectively, from the 200th cycle onwards, while B320 stayed at approximately 6.45×10^{-5}% after 50 cycles. The low ratcheting rate of B320 suggests that its behaviour is still close to elastic shakedown rather than fully activated ratcheting in LC2, especially considering that it endured a significantly higher stress range than the other two rail steels, as indicated in Table 2.

This experimental investigation confirmed that the bainitic B320 steel has markedly superior mechanical strength compared to the two pearlitic steels R220 and R260MN, particularly evident in its significantly lower plastic strain at higher stress levels for both load cases. The high yield strength of B320 bainitic rail steel is largely attributed to its distinctive microstructure, characterized by bainitic ferrite with very fine grain size and a high dislocation density (Bhadeshia 2001a), which significantly restrict dislocation movement and thereby enhance yield strength (Bhadeshia 2001b; Aglan 2004; Zhu et al., 2022). Additionally, the alloy composition, particularly the high silicon content, plays a crucial role by suppressing carbide precipitation, resulting in a predominantly carbide-free microstructure (Lesage 2022) (indicated in Table 1) that maintains both high strength and toughness (Hasan et al., 2018). Furthermore, retained austenite within the bainitic steel significantly contributes to strength enhancement through its transformation into martensite under applied stress, known as the transformation-induced plasticity effect. This martensitic transformation from the retained austenite in the bainitic steel provides additional work hardening and further boosts yield strength (Gola et al., 2017; Chen 2019), and thus reduces the accumulation of plastic strain (ratcheting) (Hasan et al., 2018). All these explain the subdued ratcheting behaviour observed in B320 during stress range tests.

Besides the high yield strength of B320, the subdued ratcheting behaviour could also be linked to the low initial plastic strain in the first load cycle. A comparison of Figs 5a and 6a reveal that the initial strain should surpass a certain threshold for significant ratcheting to occur in the following cycles. For instance, an initial strain of 1.5% can be used as a starting point to preload the specimens before the cyclic stress range test and evaluate the initial strain effects. This can be further evaluated in a pre-strain analysis via FE simulations. The initial strain effect may be

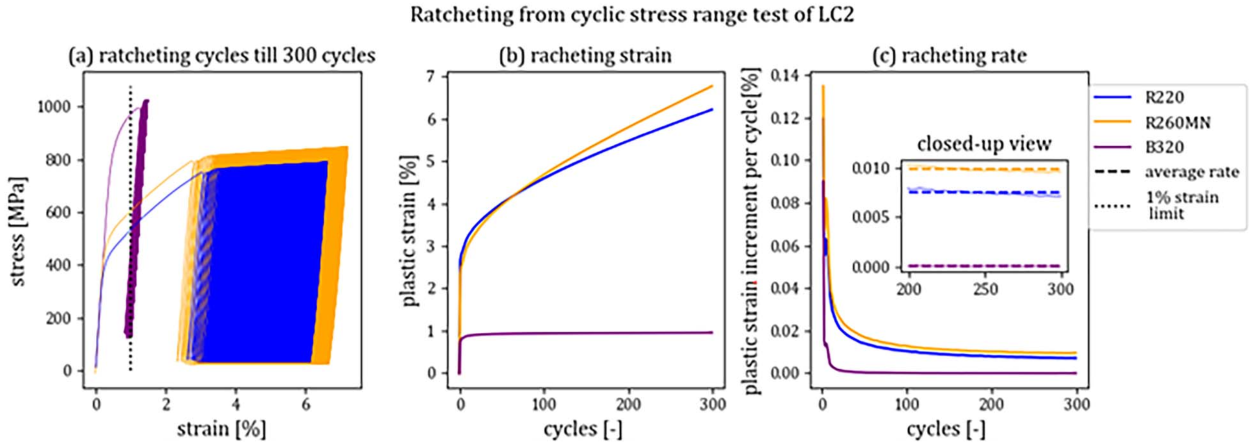

Figure 6 Cyclic stress range test results of the R220, R260MN and B320 rail steels for LC2: (a) stress-strain results till 300 cycles, (b) ratcheting strain plotted against load cycles, and (c) ratcheting rate plotted against load cycles

attributed to isotropic softening in rail steels (Kang and Gao 2002; Pun 2014) that effectively reduces yield stress (as in constitutive modelling, explained in Sections 3 and 4) with increasing effective plastic strain. The role of isotropic softening in the activation of material ratcheting merits further investigation.

Based on the test results, constitutive models can be calibrated and optimised for the three rail steels as explained in Section 2.1. These constitutive models replicate the elasto-plastic properties of the rail steels, which are crucial for simulating ratcheting effects in cyclic wheel-rail contacts. The stress-strain relationships obtained from both the monotonic and cyclic strain range tests will be utilised to calibrate the initial hardening parameters, as detailed in Section 3. Subsequently, results from cyclic stress range tests will be employed for the final optimisation of the parameters that regulate the ratcheting rate within the models.

3. Constitutive modelling

This section provided a theoretical overview of the two constitutive models featured in this study, that is the Chaboche model and the OWII model, focusing on the kinematic hardening processes described by the models. The similarities and differences between the models were highlighted. Furthermore, the isotropic hardening/softening process represented by the VOCE method was also discussed and incorporated in the constitutive models.

3.1. NLKH

NLKH properties of the rail steels have been characterised using the Chaboche (Chaboche 1986; Frederick and Armstrong 2007) and OWII constitutive models (Ohno and Wang 1993 1995). These models adhere to three fundamental rules: the yield criterion, the normality flow rule, and the hardening rule (Abdel-Karim 2009). Both the Chaboche and OWII models employ the von-Mises yield criterion, as defined by Equation (1):

$$f = \frac{3}{2}(\boldsymbol{s} - \boldsymbol{a}) : (\boldsymbol{s} - \boldsymbol{a}) - \sigma_y^2 \tag{1}$$

where the $\boldsymbol{s}$ is the deviatoric stress tensor, $\boldsymbol{a}$ is the backstress tensor and σ_y is the scalar yield stress. The yield function $f \geq 0$ 0 signifies that yield in material occurs, leading to the generation of plastic strain. The plastic strain,$\boldsymbol{\epsilon_p}$, is considered as part of the total strain, $\boldsymbol{\epsilon}$, which can be decomposed as shown below:

$$\boldsymbol{\epsilon} = \boldsymbol{\epsilon_e} + \boldsymbol{\epsilon_p} \tag{2}$$

The elastic strain,$\boldsymbol{\epsilon_e}$ in Equation (2), can be directly calculated according to Hooke's Law with the stiffness tensor, $\mathbf{C}$ multiplied by the stress tensor, $\boldsymbol{\sigma}$ (Roostaei and Jahed 2022) as shown in Equation (2).

$$\boldsymbol{\epsilon_e} = \boldsymbol{C\sigma} \tag{3}$$

The plastic strain should be determined according to the normality flow rule (Chaboche 1986; Abdel-Karim 2009) which requires that the change in plastic strains follows the gradient of the yield surface with respect to the change in stress as per Equation (4).

$$d\boldsymbol{\epsilon_p} = d\lambda \frac{\partial f}{\partial \boldsymbol{\sigma}} = \frac{3}{2}\frac{1}{h}\langle d\boldsymbol{\sigma} : \boldsymbol{n}\rangle \boldsymbol{n} \tag{4}$$

$$\boldsymbol{n} = \frac{\frac{\partial f}{\partial \boldsymbol{\sigma}}}{\sqrt{\frac{\partial f}{\partial \boldsymbol{\sigma}} : \frac{\partial f}{\partial \boldsymbol{\sigma}}}} \tag{5}$$

where $d(\cdot)$ indicates the (incremental) change of the items: $d\boldsymbol{\epsilon_p}$ is thus the incremental plastic stress tensor, $d\boldsymbol{\sigma}$ is the incremental stress tensor, and $d\lambda$ is the change in the plastic multiplier. The $\frac{\partial f}{\partial \boldsymbol{\sigma}}$ is the gradient of the yield surface. The normality flow rule can be further expanded to include the non-linear plastic modulus h, specified by the hardening rule. The $\boldsymbol{n}$ is the unit normal tensor of the gradient of the yield function according to Equation (5). The Macaulay bracket, $\langle\cdot\rangle$, returns zero when the value inside is negative. Therefore, $\langle d\boldsymbol{\sigma} : \boldsymbol{n}\rangle$ stipulates that plastic strain occurs only when the change in stress aligns with the gradient of the yield function.

The hardening rule can be formulated by introducing backstress (Abdel-Karim 2009). In the Chaboche model, the total backstress is the sum of several components specified by Equation (6). $\boldsymbol{\epsilon_p}$ is the plastic strain tensor, and p is the scalar of effective plastic strain determined by Equation (7). $\mathrm{C_i}$ and γ_{i} are the plastic modulus and the plastic strain constant for the individual component of the backstress $\boldsymbol{a_i}$. The first term of Equation (6) has the same form as Prager's linear kinematic hardening (Prager 1949). The second term features the dynamic recovery in the backstress that results in the Bauschinger effect (Chaboche 1986; Ohno and Wang 1995; Frederick and Armstrong 2007; Abdel-Karim 2009). Furthermore, by applying the consistency condition $f = df = 0$ (Chaboche 1986; Abdel-Karim 2009), the non-linear plastic modulus,h, crucial for solving the plastic strain, can be derived as shown in Equation (8).

$$d\boldsymbol{a_i} = \frac{2}{3} C_i d\boldsymbol{\epsilon_p} - \gamma_i dp \boldsymbol{a_i} \tag{6}$$

$$dp = \sqrt{\frac{2}{3} d\boldsymbol{\epsilon_p} : d\boldsymbol{\epsilon_p}} \tag{7}$$

$$h = \sum_i \left[C_i - \sqrt{\frac{3}{2}} \gamma_i \boldsymbol{n} : \boldsymbol{a_i} \right] \tag{8}$$

The backstresses of OWII model is shown in Equation (9). The OWII model shares the same linear kinematic term with the Chaboche model. The second term in Equation (9) of OWII model makes the dynamic recovery effect less active compared to the Chaboche model (Ohno and Wang 1995). The control constant m_i is introduced in each backstress component to regulate the ratcheting rate. $\overline{a_i}$ is the effective backstress calculated by Equation (10). C_i/γ_i can be interpreted as the stabilised value of each backstress component that remains constant when the plastic strain reaches $1/\gamma_i$ (Ohno and Wang 1993). The ratcheting rate is therefore controlled by multiplying a coefficient $\overline{a_i}/(C_i/\gamma_i)$ (≤ 1) by the dynamic recovery term with the m_i smaller to intensify or larger to abate its effect as shown in Equation (9). The nonlinear plastic modulus, h can then be derived as shown in Equation (11).

$$d\boldsymbol{a_i} = \frac{2}{3} C_i d\boldsymbol{\epsilon_p} - \gamma_i \left(\frac{\overline{a_i}}{C_i/\gamma_i} \right)^{m_i} \left\langle d\boldsymbol{\epsilon_p} : \frac{\boldsymbol{a_i}}{C_i/\gamma_i} \right\rangle \boldsymbol{a_i} \tag{9}$$

$$\overline{a_i} = \sqrt{\frac{3}{2} \boldsymbol{a_i} : \boldsymbol{a_i}} \tag{10}$$

$$h = \sum_i \left[C_i - \frac{3}{2} \gamma_i \left(\frac{\overline{a_i}}{C_i/\gamma_i} \right)^{m_i} \left\langle \boldsymbol{n} : \frac{\boldsymbol{a_i}}{C_i/\gamma_i} \right\rangle \boldsymbol{n} : \boldsymbol{a_i} \right] \tag{11}$$

The OWII model can be further simplified (Ohno and Wang 1995; Abdel-Karim 2009) as shown in Equation (12), which becomes the Chaboche model when $m = 0$ with a single m specified here for the simplified OWII model (Bari and Hassan 2000). The non-linear plastic modulus is thus simplified to Equation (13). The simplified OWII is used in this study to facilitate a direct comparison with the Chaboche model. Compared to the original OWII model, the simplified model uses a higher m value to control the ratcheting effects (Ohno and Wang 1995).

$$d\boldsymbol{a_i} = \frac{2}{3} c_i d\boldsymbol{\epsilon_p} - \gamma_i \left(\frac{\overline{a_i}}{C_i/\gamma_i} \right)^{m} dp \boldsymbol{a_i} \tag{12}$$

$$h = \sum_i \left[C_i - \sqrt{\frac{3}{2}} \gamma_i \left(\frac{\overline{a_i}}{C_i/\gamma_i} \right)^{m} \boldsymbol{n} : \boldsymbol{a_i} \right] \tag{13}$$

3.2. Isotropic hardening/softening

VOCE method (Voce 1955; Chaboche 1986) are also used in the aforementioned two constitutive models to approximate the isotropic hardening/softening properties of the rail steel, which evaluates the nonlinear expansion or contraction of the yield surface in response to the accumulation in the effective plastic strain as shown in Equation (14). dR is the change in the yield stress that is induced by the change in the effective plastic strain dp. R symbolises the cumulative change in the yield stress, with its upper limit defined by Q as the maximum change in yield stress when isotropic hardening or softening reaches saturation. The rate for isotropic hardening/softening saturation, is also influenced by the rate factor b (Karvan and Varvani-Farahani 2018; Nath et al., 2019) as shown in Equation (14).

$$dR = b(Q - R)dp \tag{14}$$

With the isotropic hardening/softening incorporated, the yield function is updated, as shown in Equation 15, with σ_{y0} as the initial yield stress:

$$f = \frac{3}{2} (\boldsymbol{s} - \boldsymbol{a}) : (\boldsymbol{s} - \boldsymbol{a}) - (\sigma_{y0} + R)^2 \tag{15}$$

4. Initial characterisation of rail steels

By calibrating the two constitutive models, the characterisations of the three rail steels are first discussed in this section. The initial NLKH and isotropic hardening/softening parameters for the two constitutive models were calibrated based on the test results from Stage 1 and Stage 2. The calibrated models were then used in conjunction with the normality flow rule (Equation (4) to numerically simulate the stress–strain relations in Stage 1 and 2, allowing for a comparison between the simulated and test results. In addition, the initial hardening parameters were applied in contact simulations to determine the load cases for tests at Stage 3, which is also elaborated in this section.

4.1. Material characterisation using Chaboche model

The classic Chaboche model (Chaboche 1986; Bari and Hassan 2000) with three sets of back stresses was used to characterise the rail steels. The parameters of Chaboche NLKH and isotropic hardening/softening were calibrated together in a multi-parametric non-linear least squares process as elaborated in (Curtis et al., 1974; Nocedal and Wright 1999), which used both the experimental data from the 100th stabilised cycle of the 1%-strain range test at Stage 2 (see in Fig. 4), and the monotonic tension tests at Stage 1 (see in Fig. 3). Since the tested strain range were limited by ±1%, the ultimate strength of the steels might not be captured if only the stabilised 100th cycle of Stage 2 was used, comparing Figs 3 and 4a. This was addressed by incorporating the monotonic test results of Stage 1 into the calibration process with the parameters for isotropic hardening/softening simultaneously identified. The calibration also used Young's moduli and the mean values of the yield stresses, shown in Table 3.

Figure 7 illustrates how the hardening parameters describe the isotropic softening and kinematic hardening processes in a monotonic test and were calibrated for the constitutive models. As plastic strain increases, isotropic softening reaches saturation and kinematic hardening becomes stabilised. The yield stress, σ_{y_0}, in the isotropic softening process can saturate to $\sigma_{y_0} + Q$ at relatively low plastic strain. The saturated yield stress, σ_y in isotropic softening is lower than the σ_{y_0}, as indicated by the dashed line in Fig. 7, representing a scenario where no change in σ_{y_0} ($Q = 0$) with increasing plastic strain. For kinematic hardening, each backstress component attains its stabilised value of $C_i/\gamma_i (i = 1, 2, 3)$ at the plastic strain threshold of $1/\gamma_i$, which should cover a sufficient range of the hardening process. During the calibration of the hardening parameters, the sum of the backstress components, $\sum a_i, (i = 1, 2, 3)$ (kinematic hardening process) plus the yield stress, σ_y (isotropic softening process) at each plastic strain

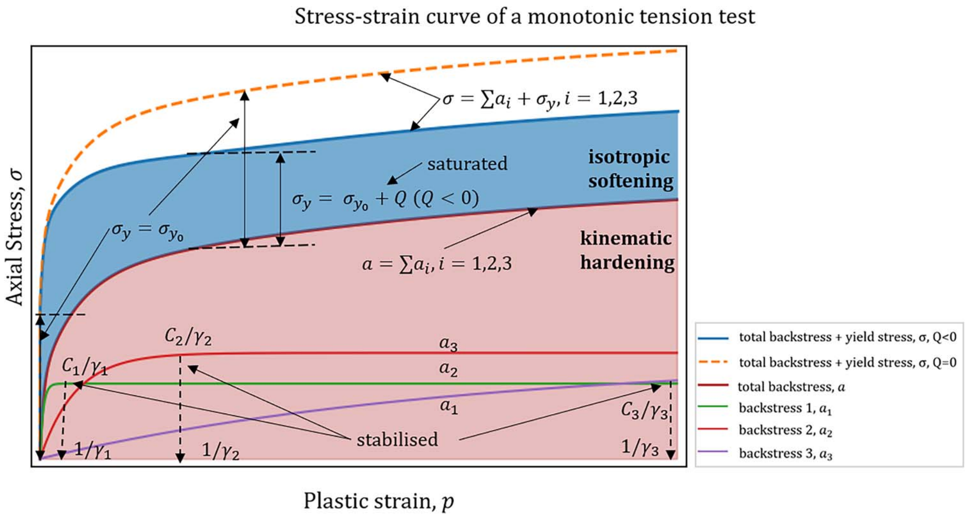

Figure 7 Illustration of isotropic softening and kinematic hardening processes in a montononic loaded stress–strain curve

Table 4. Initially calibrated hardening parameters for the Chaboche model.

Parameters	R220	R260MN	B320	Unit
C_1	511,000	461,000	522,000	
C_2	15,000	20,000	70,000	[MPa]
C_3	10,500	11,300	15,500	
γ_1	1,938	1,964	2,213	
γ_2	100	87	240	[-]
γ_3	27	28	36	
Q	−145	−167	−220	[MPa]
b	350	277	215	[-]

level approximates the total axial stress, σ and was compared with that in the test results during the calibration process.

The calibrated hardening parameters are presented in Table 4. Negative values of the parameter Q that determines the saturated yield stress in Equation (14), indicate that the three steel rails exhibit an isotropic softening process as expected (Schleinzer and Fischer 2000; Kang and Gao 2002; Pun 2014), namely the yield stress σ_y decreases with increasing equivalent plastic strain, p, until the limit $\sigma_{y0} + Q$ or saturation is reached, as illustrated in Fig. 7.

Relatively large values of C_3 ($\geq$ 10,000 MPa) were selected during the calibration process as this was found beneficial for the subsequent optimisation of the hardening parameter, γ_3 (to be discussed in Section 5). Nevertheless, the C_3 values are limited by the values of γ_3 that should not be lower than γ_2, since $1/\gamma_i$, by definition, is the plastic strain limit for the backstress component to stabilise at C_i/γ_i, as illustrated in Fig. 7 and discussed in Section 3. To use γ_3 as control constant of ratcheting, the $1/\gamma_3$ should not be too close to the tested plastic strain range, for example 1% (per load cycle) either as the third backstress component should not stabilise (Bari and Hassan 2000; Ramezansefat and Shahbeyk 2015), which also limits the value of γ_3 and thereby C_3. Furthermore, the calibration of C_3 considered the monotonic tension results in this study. It was found that a higher C_3 (basically a plastic modulus) gave a 'stiffened' response in the backstress, causing the stress calculated in the higher strain range to overshoot, as evidenced in the results of B320 (see later in Fig. 8b). Consequently, it is crucial to maintain an appropriate balance between high values of C_3 and γ_3 for optimisation of ratcheting behaviour while accurately replicating the results of the monotonic tension.

The calibrated parameters were further used to simulate the strain range tests using the numerical solution of plastic strains according to Equation (5) with Equation (8) for Chaboche or Equation (12) for OWII. The outcomes of the simulations were then evaluated against the test results from the stabilised cycle depicted in Fig. 8. A minor discrepancy was observed between the simulated and test results, particularly in the highly non-linear part of the stress-strain curve immediately following the elastic part, where no plastic strain variation occurs with increased stress as shown in Fig. 8a. This discrepancy corresponds with the findings reported in (Bari and Hassan 2000; Nath et al., 2019). Additionally, the comparisons between the monotonic tension simulations and tests in Fig. 8b indicated that the calibrated models achieved stress levels close to the ultimate strength. Discrepancies in B320 can be seen between the simulated and monotonic test results, attributed to the high value of C_3 as previously discussed.

4.2. Material characterisation using OWII model

The calibration of the OWII model is normally more straightforward, since hardening parameters can be directly determined from monotonic test data when the isotropic hardening/softening is not significant (Ohno and Wang 1993; Bari and Hassan 2000). This is usually not the case for rail steels that experience significant isotropic softening, as discussed above. Conveniently, backstresses can be obtained by subtracting the yield stresses at each plastic strain level from the monotonic test data (indicated in Fig. 7), since isotropic softening has already been characterised together with the Chaboche model. The remaining (ratcheting) control constant, m (Equation (12)), can be determined depending on the load cases in the later optimisation process (to be discussed in Section 5).

Table 5 provides a summary of the OWII hardening parameters calibrated for the three rail steels. Different from the Chaboche model, the exponential shape of the stress–strain relation (see Fig. 7) replicated by the OWII model (effectively a Chaboche model when $m = 0$, discussed in Section 3), can become multi-linear (Abdel-Karim and Ohno 2000; Bari and Hassan 2000), that is

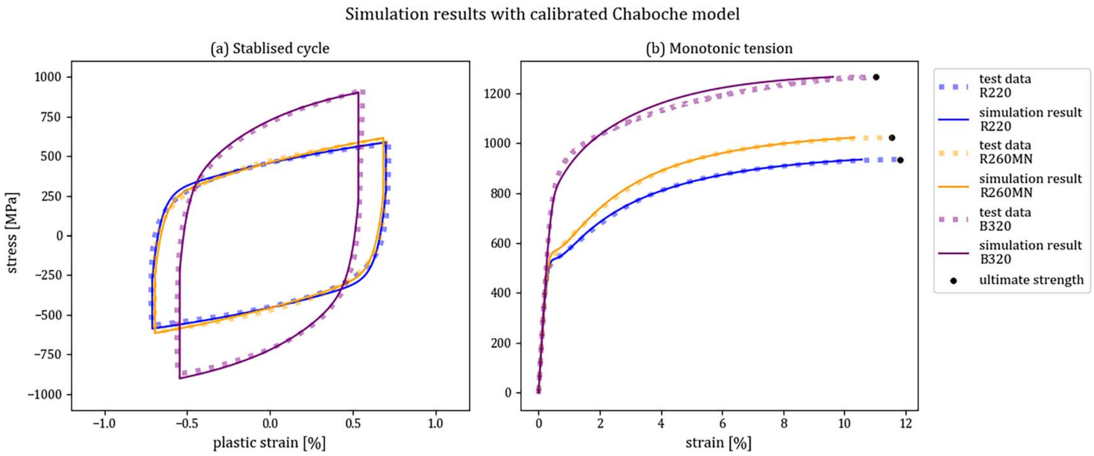

Figure 8 Simulation results compared with test results of the R220, R260MN and B320 rail steels based on Chaboche model: (a) the stabilised cycle of 1% strain range cyclic test, and (b) the monotonic tension test till ultimate strength

Table 5. Initially calibrated hardening parameters for OWII model.

Parameters	R220	R260MN	B320	Unit
C_1	725,000	365,000	800,000	
C_2	76,000	52,000	251,000	
C_3	26,800	15,100	53,500	
C_4	86,00	7,000	18,200	[MPa]
C_5	4,200	5,800	8,000	
C_6	3,800	4,800	3,400	
C_7	2,300	2,900	2,600	
γ_1	5,133	2,850	8,429	
γ_2	1,175	632	1,492	
γ_3	394	231	408	
γ_4	100	111	130	[MPa]
γ_5	47	51	74	
γ_6	25	29	29	
γ_7	13	13	13	
Q	−145	−167	−220	[MPa]
b	350	277	215	[-]

composing several linear sections, with a larger value of m (e.g. ≥ 1), as shown in Fig. 9a. Therefore, more sets of hardening parameters (C_i and γ_i) are required to closely replicate the nonlinear part of the stress–strain curve. In this study, seven sets were used to balance the computational efficiency for future FE simulations of wheel–rail contacts using constitutive models in rail material, and accuracy of reproducing the constitutive/stress–strain relation, as shown in Fig. 9. Figure 9a shows a reasonable match between the numerical simulation results of OWII model and the strain range test results for the three rail steels. By comparing the simulation results with $m = 1$ and $m = 5$, we can see that the m value can alter the shape of the stress-strain curve in Fig. 9a, and change the monotonic responses in Fig. 9b as a higher m value can 'stiffen' the material, resulting in a reduced strain value at higher stress levels for the steels.

4.3. Load case determination for stress range tests

Two load cases (Table 2) for the cyclic stress range tests at Stage 3 were determined based on two contact conditions. The stress ranges in these load cases were determined from wheel–rail contact simulations using an FE wheel–rail contact model (Ren et al., 2024), where the initially calibrated Chaboche model (Table 4) was applied in the rail material. The FE model duplicated the test setup of the V-track (Naeimi 2017; Zhang et al., 2021), a scaled test rig used to reproduce real-life wheel–rail contact conditions and the consequent phenomena (Yang 2022; He 2024; Ren et al., 2025). A normal load of 3,500N and a traction coefficient (μ) of 0.3 were applied in the FE model as LC1, to produce a partial-slip rolling contact condition on the V-Track for ratcheting and RCF generation (Ren et al., 2025), considering that the friction coefficient of the V-Track rail is 0.45 under a dry and clean condition. For comparison, the second load case, LC2, produced a full-slip contact condition with a traction coefficient equal to the friction coefficient, which achieves higher shear stresses and consequently a higher equivalent stress level during the contact.

Figure 10 illustrates the simulated contact shear stresses and traction bounds for both load cases on the rails. In Fig. 10a, the adhesion and slip regions can be identified in the partial-slip contact solutions: the shear stresses are below and equal to the traction bounds in the adhesion and slip regions, respectively. Verifcaiton of the FE solution against CONTACT, widely-accepted software for rolling contact solutions (Kalker 1991), has been reported in (Ren et al., 2024). In both Fig. 10a and b, the peak pressures are not in the centre but shifts to the leading part, corresponding well to the plastic contact pressure distribution in (Wei 2015).

Figures 11 and 12 demonstrate how the loading pattern for the stress range tests were determined for the LC1 and LC2 in Table 2, respectively. The cyclic contact simulation was run to obtain the equivalent stress levels before and during rolling contact. Only two load cycles were simulated to avoid the possible influence of ratcheting that was not yet considered in the calibration of constitutive models at Stage 2. The peak equivalent stresses were obtained from the highest stress levels loaded by the contact in the first cycle. Subsequently, the residual equivalent stresses were obtained before the contact in the second cycle, representing the stress levels unloaded from contact after the first cycle. The loaded and unloaded stress levels (in Table 2) can then be determined as the levels of the peak and residual equivalent stresses, respectively, as indicated by the red dash-dotted lines in Figs 11 and 12. The loading patterns for cyclic stress range tests were subsequently constructed as the cyclic triangular ramp loads (solid red lines in Figs 11 and 12), which basically match the equivalent stresses induced by wheel–rail

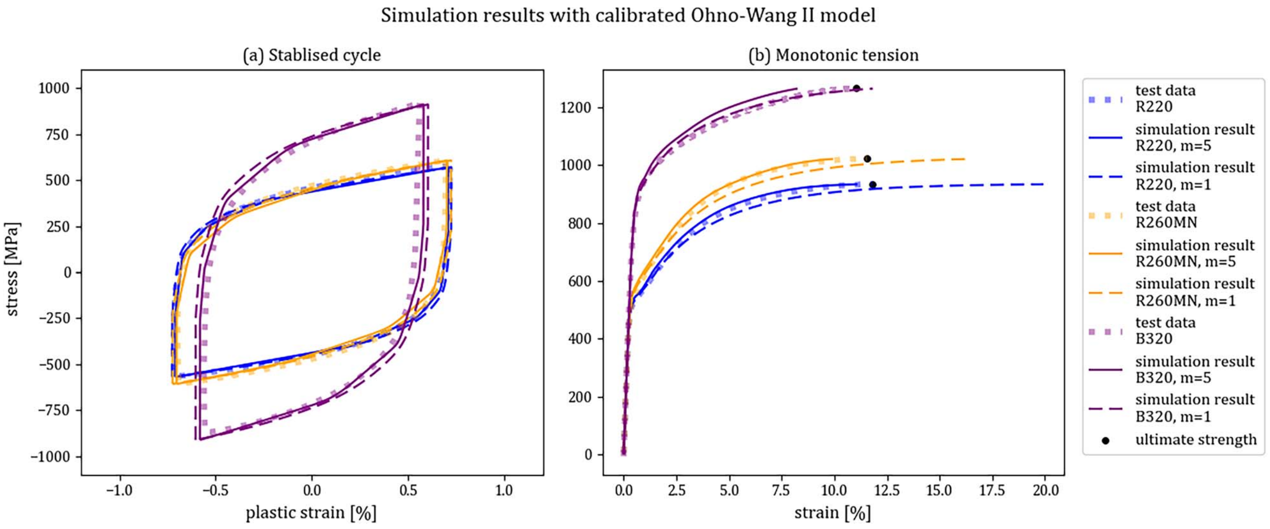

Figure 9 Simulation results compared with test results of the R220, R260MN, and B320 rail steels based on OWII model: (a) the stablised cycle of 1% strain range cyclic test, and (b) the monotonic tension test till ultimate strength

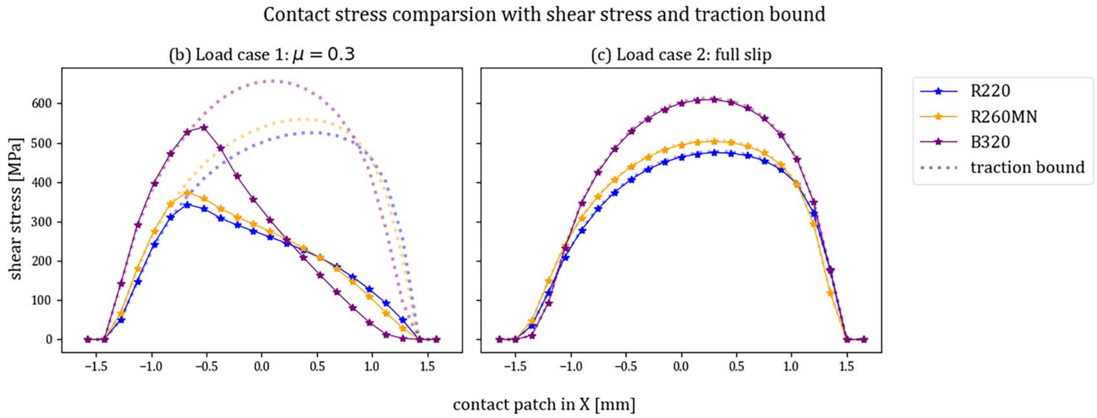

Figure 10 Comparison of the contact shear stresses and traction bounds for R220, R260MN and B320: (a) the results from LC1, and (b) the results from LC2

contact loading conditions. This replication of wheel–rail contact-induced stresses facilitated testing of the rails close to railway operating conditions and comparison of the three rail steels for their ratcheting behaviours, considering the significant difference in their mechanical strengths.

5. Constitutive model optimisation for ratcheting

This section presents the optimisation process of the calibrated constitutive models for better representations of the rail material ratcheting properties. The material ratcheting behaviour of the rail steels prior to optimisation was first compared with the test results of Stage 3. Subsequently, the relevant parameters for both constitutive models were adjusted to align the calculated ratcheting strains and rates with those of the test results. Accordingly, material ratcheting behaviour simulated with the optimised constitutive models was presented and compared with the relevant/corresponding test results at Stage 3.

5.1. Material ratcheting simulated with initial hardening parameters

Figure 13 compares the ratcheting strains obtained with cyclic stress range tests (shown also in Fig. 5a and b) to the results simulated using two constitutive models, that is Chaboche and OWII, with the initial hardening parameters calibrated in Sections 4.1 and 4.2. Here, the simulations refer to the numerical simulations that solve the plastic strains following Equation 5 with Equation 8 for Chaboche, or Equation 13 for OWII, under the same stress ranges tested at Stage 3.

An outlier of the ratcheting strain results can be observed in Fig. 13c that the B320 rail, for LC1, exhibited an elastic shakedown effect (Paul 2019) during which the ratcheting rate diminished after about eight load cycles. This has been noticed in Fig. 5c: the ratcheting rate was reduced to a very low level after only a few testing load cycles. In Fig. 13c, the ratcheting strain calculated with the Chaboche model matched closely with the test result, while the result of OWII model had a lower plastic strain level but still reached the shakedown after the eighth load cycle. This misalignment can be attributed to the ratcheting control constant, for example a larger m (≥ 1) that makes the material 'stiffer' and produces smaller strain values, as discussed in Section 4.2. Nonetheless, the difference in plastic strain was comparably small at about 0.15%.

5.2. Optimisation of the constitutive models

In the optimisation process, the relevant parameters were iterated in the numerical simulations (discussed in Section 4.1) of

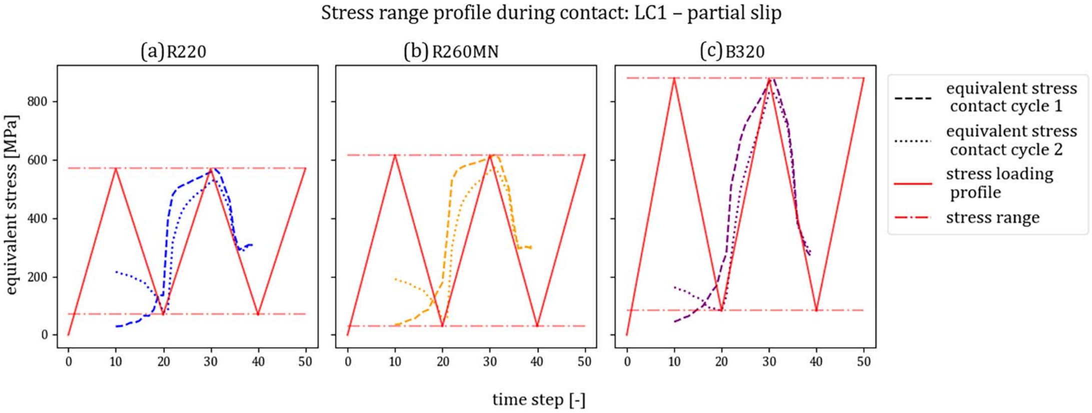

Figure 11 Stress ranges of LC1, determined based on the simulated equivalent stresses of two wheel-rail partial-slip contacts (a) R220, (b) R260MN, and (c) B320

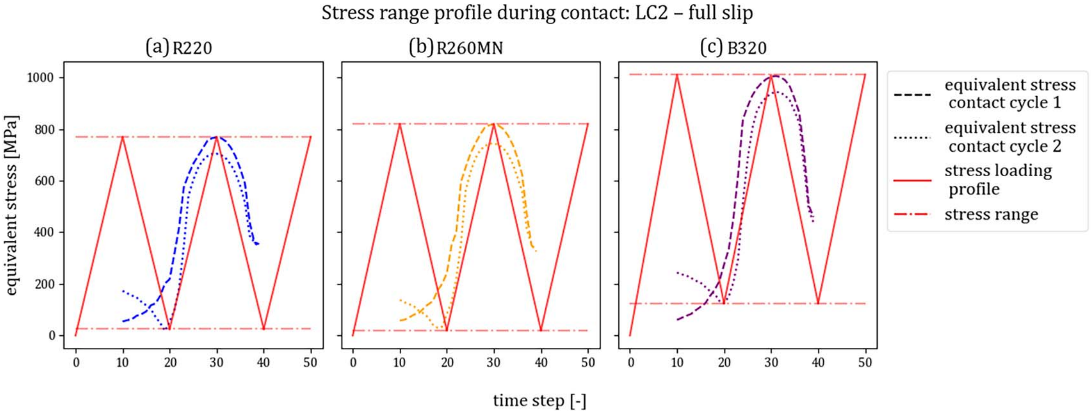

Figure 12 Stress ranges of LC2, determined based on the simulated equivalent stresses of two wheel-rail full-slip contacts (a) R220, (b) R260MN, and (c) B320

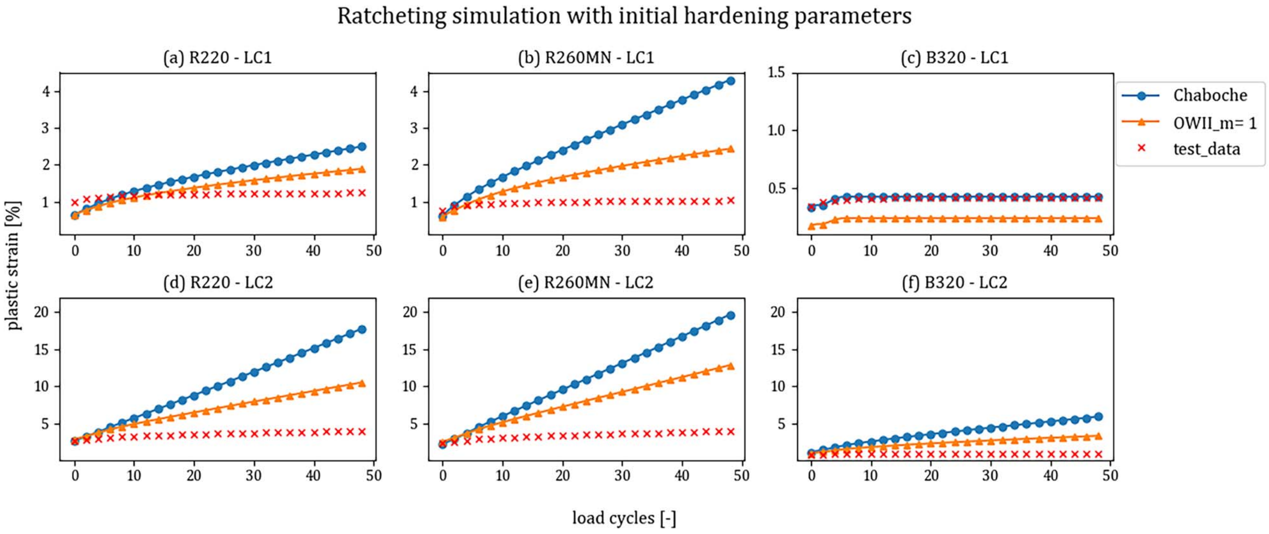

Figure 13 Ratcheting simulation results using the inital parameters of Chaboche and OWII ($m = 1$) compared with the test data for LC1 and LC2: (a) R220 under LC1, (b) R260MN under LC1, (c) B320 under LC1, (d) R220 under LC2, (e) R260MN under LC2, and (f) B320 under LC2

the cyclic stress range tests to match the simulated and tested ratcheting rates as suggested in (Bari and Hassan 2000). The initial hardening parameter, γ_3, should be reduced for the Chaboche model (Bari and Hassan 2000), whereas the control constant, m, was increased for OWII model (Ohno and Wang 1995; Bari and Hassan 2000), to reduce the simulated ratcheting rates. In this study, γ_3 or m was optimised separately for each load case, instead of looking for a single value to work for both load cases, as this has been found difficult according to (Bari and Hassan 2000; Ramezansefat and Shahbeyk 2015) and also in this study. Therefore, different values of γ_3 and m were presented for LC1 and LC2.

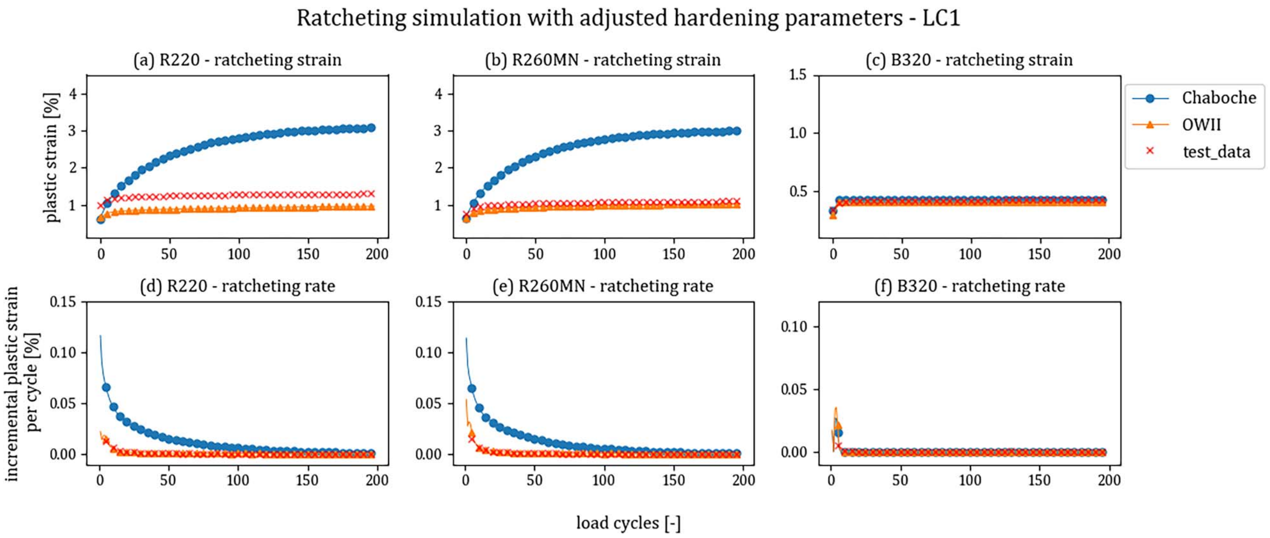

Figure 14 Ratcheting simulation results using the adjusted parameters of Chaboche and OWII compared with the test data for LC1: (a)–(c) the comparison of racheting strains for R220, R260MN, and B320, and (d)–(f) the comparison of racheting rates for R220, R260MN, and B320

Table 6. Adjusted hardening parameter of Chaboche and control constant of OWII models for LC1.

Parameters	R220	R260MN	B320
γ_3	0.0001	0.0001	36.00
m	27.00	31.00	0.00

Table 7. Adjusted hardening parameter of Chaboche and control constant of OWII models for LC2.

Parameters	R220	R260MN	B320
γ_3	1.06	1.05	0.0001
m	10.30	9.00	85.00

The optimised parameters γ_3 and m for LC1 are shown in Table 6. The rail steels exhibited relatively low ratcheting rates in LC1 as discussed in Section 2.4, which resulted in extremely low γ_3 values for the Chaboche models and relatively high m values for the OWII model, except for B320. Since the B320 was in elastic shakedown, the Chaboche parameters were unchanged. Comparisons between the tested and simulated ratcheting strains using optimised hardening parameters are presented in Fig. 14. The parameter m for the OWII model was reduced to 0 (effectively becoming a Chaboche model) to better match the level of plastic strain of the test, as shown in Fig. 14c.

Figures 14a and b show the simulated ratcheting strains compared with the test results for R220 and R260MN. For both rail steels, the ratcheting strains simulated with the optimised Chaboche model overshot to a level above 3% after 200 cycles, while the test results achieved strains slightly above 1%. With very small values γ_3 (= 0.0001), the simulated ratcheting rates could approach a level similar to the test results approaching 150 cycles, as shown in Fig. 14d and e. In contrast, the optimised OWII model performed better than the Chaboche model as indicated in Fig. 14a, b, d, and e with a close match in the ratcheting rates achieved between the simulated and test results. For the ratcheting strains, despite the initial difference in the strain level of R220 (Fig. 14a), the patterns of the simulated strain accumulation were well aligned with the test results.

In contrast to R220 and R260MN, B320 steel exhibited elastic shakedown in LC1, as shown in Fig. 14c and f, owing to its high mechanical strength. The simulation results using both constitutive material models demonstrated the shakedown behaviour. Figure 14c shows that the Chaboche model with the initial calibrated hardening parameters could reproduce the matching ratcheting strains from the test without γ_3 being adjusted. The optimised OWII model can also produce the ratcheting strain pattern obtained with tests for B320 but with a small gap (about 0.05%) at the first cycle. In line with test results, the ratcheting rates calculated with the optimised models stabilised and reached zero after the first cycles, as shown in Fig. 14f.

The optimised parameters for LC2 are provided in Table 7 and the corresponding simulation results of material ratcheting behaviour are presented in Fig. 6. For the R220 and R260MN steels, the optimised parameters γ_3 for the Chaboche model under LC2 are larger than those under LC1, while the optimised parameters m for the OWII model are smaller under LC2. As shown in Fig. 15a, b, d, and e, the ratcheting strains and rates simulated with the optimised models match reasonably well with the test results. The optimised OWII model performed excellently with the simulated ratcheting strains and rates both matching closely with the test results. The optimised Chaboche model also demonstrated the improved accuracy in predicting the rail ratcheting behaviour for LC2, although the ratcheting strains and rates were not precisely aligned with test results before 50 cycles.

The performance improvement of the Chaboche model in predicting ratcheting behaviour of R220 and R260MN can be attributed to two factors. First, the material ratcheting effects observed for R220 and R260MN steels were significantly more pronounced in LC2 than in LC1, reducing the need to lower the γ_3 values substantially to align with the ratcheting rates observed in the tests. Second, during the calibration of the initial NLKH parameters, high values were purposely selected for C_3, and consequently also for γ_3, giving more flexibility in its adjustment. Comprehensively comparing the simulation results under LC1 and LC2, it can be concluded that the Chaboche model struggled to accurately reproduce rail ratcheting behaviour with low ratcheting rates due to its relatively simple form in the nonlinear part of the kinematic hardening (see in Equation (6)); in

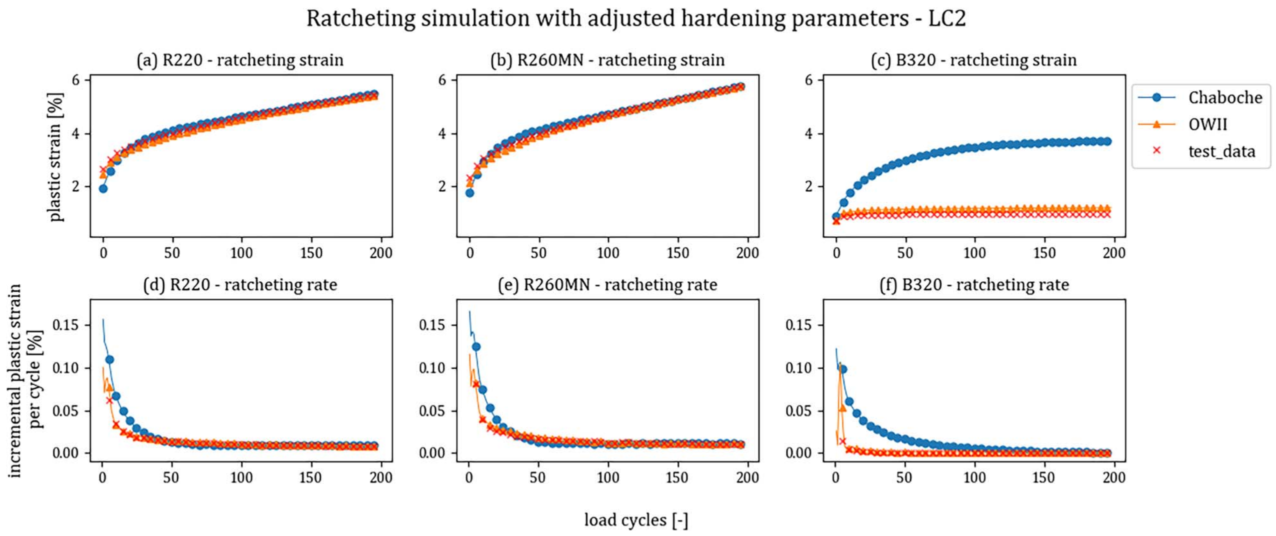

Figure 15 Ratcheting simulation results using the adjusted parameters of Chaboche and OWII compared with the test data for LC2: (a)-(c) the comparison of racheting strains for R220, R260MN and B320, and (d)-(f) the comparison of racheting rates for R220, R260MN and B320

contrast, the OWII model exhibited better adaptiveness to varying ratcheting rates, facilitated by direct adjustments of the control constant, m, (Equation (12) in the model.

For the B320 steel of LC2, the stabilised ratcheting rate observed during the test was still nearly negligible ($< 10^{-4}$%), and the stabilised ratcheting rate remained very low, which was close to a shakedown. Fig. 15c and f indicate that the optimised Chaboche model faced limitations in predicting the ratcheting behaviour of B320 under LC2 with low ratcheting rates, especially in the first few load cycles, as discussed above. The simulation approximated the test ratcheting rate after about 150 cycles, as shown in Figs 15 and 14f. Meanwhile, the optimised OWII model also had difficulty replicating the ratcheting behaviour of B320, leading to a notably high level of $m = 85$. A possible reason is that the yield stress of the tested sample could be at the upper bound of its variation range, while the mean value was used in the calibration (see Table 3). In such a case with the higher yield stress, the test can result in a shakedown state (e.g. for B320 under LC2), and the ratcheting behaviour cannot be correctly captured by the constitutive models calibrated based on the mean yield stress. These observations underscore that more extensive tests of the B320 rail material are needed to better represent its ratcheting behaviour using the Chaboche and OWII constitutive models (to be discussed in further research).

6. Conclusion and further research

This study experimentally investigated the mechanical, hardening, and material ratcheting properties of three different rail steels: R220, R260MN, and B320. The testing process was structured into three stages: the monotonic tension tests, cyclic strain range tests, and cyclic stress range tests. The load cases of the cyclic stress range tests were determined based on FE wheel–rail contact simulations to reflect the variation in equivalent stresses on the rail top surface in practice. Test results revealed that the bainitic steel B320 possesses superior mechanical strengths compared to the pearlitic steels R220 and R260MN, exhibiting higher yield stress and ultimate strength. Additionally, B320 showed much less significant ratcheting behaviour in the two applied load cases representing partial-slip and full-slip wheel–rail contact, respectively, in contrast to the pearlitic steels, demonstrating superior resistance to ratcheting and RCF, and thereby potentially extending rail service life. The R220 and R260MN rails demonstrated similar mechanical strengths, with R260MN being slightly stronger, and similar ratcheting behaviours in both load cases. The test outcomes were then utilised to calibrate and optimise the hardening parameters of the Chaboche and OWII constitutive models. The comparisons between the test and simulation results using the optimised constitutive models indicated that the Chaboche model is reasonably accurate in modelling the shakedown behaviours for the bainitic B320 and the ratcheting behaviours at high ratcheting rates for the pearlitic R220 and R260MN rail steels, but less adaptive for simulating the ratcheting behaviours at low ratcheting rates for the three rail steels; the OWII model, in contrast, exhibited better performance in terms of rail shakedown and ratcheting behaviour modelling for all three rail types and for both load cases.

All the three tested rail steels have experienced material ratcheting during the cyclic stress range tests, especially in the LC2 that produced the equivalent stress condition of a full-slip wheel-rail contact. However, the material ratcheting of the B320 steel was much less pronounced, as it was in elastic shakedown in LC1, and still close to a shakedown state in LC2. The subdued ratcheting behaviours could be attributed to the relatively low initial plastic strain of the B320 in the first cycle (because of the high yield stress of B320), which remained below 1%, possibly limiting the isotropic softening of the rail steel and the subsequent material ratcheting behaviour. Therefore, for a better understanding and representation of the ratcheting characteristics of the B320 bainitic rail steel, it would be beneficial to conduct the following complementary tests:

- First yield the B320 steel to a pre-strain of for example 1.5% (to be determined based on FE contact simulation) to possibly saturate the isotropic softening, and then use the yielded material in the uniaxial cyclic stress range test under the same stress ranges determined in this study.
- Include torsion loading in a bi-axial cyclic stress range test of B320, using shear stresses to induce a higher effective plastic strain under compressive and shear stress ranges that are equivalent to the stress ranges used in this study.
- Use higher stress ranges to induce higher plastic strains and compare B320 with premium rail steel grades such as

MHH (head-hardened pearlitic) or B360 (bainitic), which have comparable or higher mechanical strengths.

Moreover, this study focused mainly on the uniaxial ratcheting behaviour of rail steels. However, the bi-axial stress conditions can produce different ratcheting behaviours in steels. Without addressing the bi-axial stress conditions may thus limit the accuracy of the constitutive models in replicating these behaviours (Ohno and Wang 1993; Abdel-Karim and Ohno 2000). Therefore, it is recommended to extend the experimental investigation to biaxial tests to further enhance the understanding of the ratcheting behaviours of the rail steels in practice and also to assess the precision of the Chaboche and OWII models to predict the ratcheting behaviours of the three rail steels under bi-axial conditions.

Acknowledgements

This study is part of the Maximise the rail Life (MaxLife) project, conducted at Delft University of Technology. The MaxLife research project (Code: 15796) was funded by the Dutch Research Council (NWO) and Dutch rail infrastructure manager, ProRail.

Author contributions

Fang Ren (Formal Analysis, Methodology, Writing—original draft), Zhen Yang (Writing–review & editing), Zili Li (Writing–review & editing).

References

Abdel-Karim, M. (2009) ‘Modified Kinematic Hardening Rules for Simulations of Ratchetting’, *International Journal of Plasticity*, **25**: 1560–1587.

Abdel-Karim, M., and Ohno, N. (2000) ‘Kinematic Hardening Model Suitable for Ratchetting with Steady-State’, *International Journal of Plasticity*, **16**: 225–240.

Aglan, H et al. (2004) ‘Mechanical and Fracture Behavior of Bainitic Rail Steel’, *Journal of Materials Processing Technology*, **151**: 268–274.

Athukorala, A. C., Pellegrin, D. V. D. and Kourousis, K. I. (2016) ‘Characterisation of Head-Hardened Rail Steel in Terms of Cyclic Plasticity Response and Microstructure for Improved Material Modelling’, *Wear*, **366-367**: 416–424.

Bari, S., and Hassan, T. (2000) ‘Anatomy of Coupled Constitutive Models for Ratcheting Simulation’, *International Journal of Plasticity*, **16**: 381–409.

Bhadeshia, H. K. D. H. (2001a Ch. Chapter 2 Bainitic Ferrite) *Bainite in Steels*, 2nd edn, pp. 19–61, London: IOM Communications.

Bhadeshia, H. K. D. H. (2001b Ch. Chapter 18 Mechanical properties) *Bainite in Steels*, pp. 285–342, London: IOM Communications.

Bower, A., and Johnson, K. (1989) ‘The Influence of Strain Hardening on Cumulative Plastic Deformation in Rolling and Sliding Line Contact’, *Journal of the Mechanics and Physics of Solids*, **37**: 471–493.

Bower, A., and Johnson, K. (1991) ‘Plastic Flow and Shakedown of the Rail Surface in Repeated Wheel-Rail Contact’, *Wear*, **144**: 1–18.

Chaboche, J. (1986) ‘Time-Independent Constitutive Theories for Cyclic Plasticity’, *International Journal of Plasticity*, **2**: 149–188.

Chaboche, J. (1991) ‘On some Modifications of Kinematic Hardening to Improve the Description of Ratchetting Effects’, *International Journal of Plasticity*, **7**: 661–678.

Chen, Y et al. (2019) ‘Microstructure Evolution of Rail Steels under Different Dry Sliding Conditions: a Comparison between Pearlitic and Bainitic Microstructures’, *Wear*, **438-439**: 203011.

Curtis, A. R., Powell, M. J. D. and Reid, J. K. (1974) ‘On the Estimation of Sparse Jacobian Matrices’, *IMA Journal of Applied Mathematics*, **13**: 117–119.

Donzella, G et al. (2005) ‘The Competitive Role of Wear and RCF in a Rail Steel’, *Engineering Fracture Mechanics*, **72**: 287–308.

Eadie, D. T et al. (2008) ‘The Effects of Top of Rail Friction Modifier on Wear and Rolling Contact Fatigue: Full-Scale Rail-Wheel Test Rig Evaluation, Analysis and Modelling’, *Wear*, **265**: 1222–1230.

Esveld, C. (2001 The Rail 2001 Nieuwhuizen, Dior Zwarthoed-van (Editor) Modern railway track, second edition Chapter 10 MRT productions (publisher) p. 275–332.

Fletcher D., Franklin F., A. Kapoor, *Rail Surface Fatigue and Wear*, Elsevier, 2009, Ch. Chapter 9, pp. 280–310, Woodhead Publishing, Cambridge. https://doi.org/10.1533/9781845696788.1.280.

Frederick, C. O., and Armstrong, P. J. (2007) ‘A Mathematical Representation of the Multiaxial Bauschinger Effect’, *Materials at High Temperatures*, **24**: 1–26.

Gola, A., Ghadamgahi, M. and Ooi, S. (2017) ‘Microstructure Evolution of Carbide-Free Bainitic Steels under Abrasive Wear Conditions’, *Wear*, **376-377**: 975–982.

Hajizad, O et al. (2019) ‘Influence of Microstructure on Mechanical Properties of Bainitic Steels in Railway Applications’, *Metals*, **9**: 778.

Hasan, S. M., Chakrabarti, D. and Singh, S. B. (2018) ‘Dry Rolling/Sliding Wear Behaviour of Pearlitic Rail and Newly Developed Carbide-Free Bainitic Rail Steels’, *Wear*, **408-409**: 151–159.

He, C et al. (2024) ‘A Finite Element Thermomechanical Analysis of the Development of Wheel Polygonal Wear’, *Tribology International*, **195**: 109577.

Hu, Y et al. (2021) ‘Microstructure Evolution of Railway Pearlitic Wheel Steels under Rolling-Sliding Contact Loading’, *Tribology International*, **154**: 106685.

Hübel, H. (1996) ‘Basic Conditions for Material and Structural Ratcheting’, *Nuclear Engineering and Design*, **162**: 55–65.

Jiang, Y., and Sehitoglu, H. (1996) ‘Modeling of Cyclic Ratchetting Plasticity, Part I: Development of Constitutive Relations’, *Journal of Applied Mechanics*, **63**: 720–725.

Kalker, J. (1991) ‘Wheel-Rail Rolling Contact Theory’, *Wear*, **144**: 243–261.

Kang, G., and Gao, Q. (2002) ‘Uniaxial and Non-proportionally Multiaxial Ratcheting of u71mn Rail Steel: Experiments and Simulations’, *Mechanics of Materials*, **34**: 809–820.

Karvan, P., and Varvani-Farahani, A. (2018) ‘Isotropic-Kinematic Hardening Framework to Assess Ratcheting Response of Steel Samples Undergoing Asymmetric Loading Cycles’, *Fatigue & Fracture of Engineering Materials & Structures*, **42**: 295–306.

Lesage, T et al. (2022) ‘Head Check Resistance of b320 Bainitic Rail Steel Grade’, *Materials Today Communications*, **31**: 103259.

Naeimi, M et al. (2017) ‘Development of a New Downscale Setup for Wheel-Rail Contact Experiments under Impact Loading Conditions’, *Experimental Techniques*, **42**: 1–17.

Nath, A., Ray, K. K. and Barai, S. V. (2019) ‘Evaluation of Ratcheting Behaviour in Cyclically Stable Steels through Use of a Combined Kinematic-Isotropic Hardening Rule and a Genetic Algorithm Optimization Technique’, *International Journal of Mechanical Sciences*, **152**: 138–150.

Nocedal, J., and Wright, S. J. (1999) *Numerical Optimization*. Springer: New York.

Ohno, N., and Wang, J. (1995) ‘On Modelling of Kinematic Hardening for Ratcheting Behaviour’, *Nuclear Engineering and Design*, **153**: 205–212.

Ohno, N., and Wang, J.-D. (1993) 'Kinematic Hardening Rules with Critical State of Dynamic Recovery, Part i: Formulation and Basic Features for Ratchetting Behavior', *International Journal of Plasticity*, **9**: 375–390.

Paul, S. K. (2019) 'A Critical Review of Experimental Aspects in Ratcheting Fatigue: Microstructure to Specimen to Component', *Journal of Materials Research and Technology*, **8**: 4894–4914 https://www.sciencedirect.com/science/article/pii/S2238785419300900.

Pletz, M et al. (2019) 'Cyclic Plastic Deformation of Rails in Rolling/Sliding Contact –Quasistatic FE Calculations Using Different Plasticity Models', *Wear*, **436-437**: 202992.

Prager, W. (1949) 'Recent Developments in the Mathematical Theory of Plasticity', *Journal of Applied Physics*, **20**: 235–241.

Pun, C. L et al. (2014) 'Ratcheting Behaviour of High Strength Rail Steels under bi-Axial Compression–Torsion Loadings: Experiment and Simulation', *International Journal of Fatigue*, **66**: 138–154.

Pun, C. L et al. (2015) 'An Efficient Computational Approach to Evaluate the Ratcheting Performance of Rail Steels under Cyclic Rolling Contact in Service', *International Journal of Mechanical Sciences*, **101-102**: 214–226.

Ramezansefat, H., and Shahbeyk, S. (2015) 'The Chaboche Hardening Rule: a re-Evaluation of Calibration Procedures and a Modified Rule with an Evolving Material Parameter', *Mechanics Research Communications*, **69**: 150–158.

Ren, F., Yang, Z. and Li, Z. (2024) 'An Efficient 3d Finite Element Procedure for Simulating Wheel–Rail Cyclic Contact and Ratcheting', *Tribology International*, **198**: 109878.

Ren, F., Yang, Z. and Li, Z. (2025) 'Experimental and Numerical Investigation into Rolling Contact Fatigue Crack Initiation on the v-Track Test Rig', *Engineering Failure Analysis*, **170**: 109206.

Ringsberg, J. (2000) 'Prediction of Fatigue Crack Initiation for Rolling Contact Fatigue', *International Journal of Fatigue*, **22**: 205–215.

Roostaei A. A., Jahed H. (Eds.), *Cyclic Plasticity of Metals*, Elsevier, 2022. https://doi.org/10.1016/c2018-0-04874-4.

Schleinzer, G., and Fischer, F. (2000) 'Residual Stresses in New Rails', *Materials Science and Engineering: A*, **288**: 280–283.

Stock, R., and Pippan, R. (2011) 'RCF and Wear in Theory and Practice—The Influence of Rail Grade on Wear and RCF', *Wear*, **271**: 125–133.

Su, H et al. (2019) 'Numerical Study on the Ratcheting Performance of Heavy Haul Rails in Curved Tracks', *Wear*, **436-437**: 203026.

Tyfour, W. R., Beynon, J. H. and Kapoor, A. (1996) 'Deterioration of Rolling Contact Fatigue Life of Pearlitic Rail Steel Due to Dry-Wet Rolling-Sliding Line Contact', *Wear*, **197**: 255–265.

Voce, E. (1955) 'A Practical Strain Hardening Function', *Metallurgia*, **51**: 219–226.

Wei, Z et al. (2015) '3d fe Modelling and Validation of Frictional Contact with Partial Slip in Compression-Rolling Evolution', *International Journal of Rail Transportation*, **4**: 20–36.

Wu, B et al. (2023) 'Study on Corrugated Wear on High-Speed Railways Based on an Improved Finite Element Model of Wheel-Rail Rolling Contact', *Tribology International*, **179**: 108199.

Wu, Y et al. (2024) '3d Rolling Contact Finite Element Analysis of High-Speed Railway Turnout Considering Ratchetting Effect', *Engineering Failure Analysis*, **160**: 108171.

Yang, Z et al. (2022) 'An Experimental Study on the Effects of Friction Modifiers on Wheel–Rail Dynamic Interactions with Various Angles of Attack', *Railway Engineering Science*, **30**: 360–382.

Zhang, P., Moraal, J. and Li, Z. (2021) 'Design, Calibration and Validation of a Wheel-Rail Contact Force Measurement System in V-Track', *Measurement*, **175**: 109105. doi: https://doi.org/10.1016/j.measurement.2021.109105.

Zhou, Y et al. (2014) 'Field and Laboratory Investigation of the Relationship between Rail Head Check and Wear in a Heavy-Haul Railway', *Wear*, **315**: 68–77.

Zhu, J., Barber, G. and Sun, X. (2022) 'Effects of Isothermal Temperature on Dislocation Density in Bainite Transformation of 4140 Steel', *Materials*, **15**: 6066.

Intelligent Transportation Infrastructure, 2025, liaf011
https://doi.org/10.1093/iti/liaf011
Research Article